Published in final edited form as:

IEEE Trans Ultrason Ferroelectr Freq Control. 2022 August ; 69(8): 2437–2446. doi:10.1109/TUFFC.2022.3180980.

Actuated Reflector-Based Three-dimensional Ultrasound Imaging with Synthetic Aperture Focusing

Yichuan Tang,
Department of Robotics Engineering, Worcester Polytechnic Institute, Worcester, MA 01609 USA

Ryosuke Tsumura [Member, IEEE],
Department of Robotics Engineering, Worcester Polytechnic Institute, Worcester, MA 01609 USA

Jakub T. Kaminski,
Department of Robotics Engineering, Worcester Polytechnic Institute, Worcester, MA 01609 USA

Haichong K. Zhang [Member, IEEE]
Department of Biomedical Engineering, Computer Science, and Robotics Engineering, Worcester Polytechnic Institute, Worcester, MA 01609 USA

Abstract

Three-dimensional (3D) ultrasound (US) imaging addresses the limitation in field-of-view (FOV) in conventional two-dimensional (2D) US imaging by providing 3D viewing of the anatomy. 3D US imaging has been extensively adapted for diagnosis and image-guided surgical intervention. However, conventional approaches to implement 3D US imaging require either expensive and sophisticated 2D array transducers or external actuation mechanisms to move a one-dimensional array mechanically. Here, we propose a 3D US imaging mechanism using actuated acoustic reflector instead of the sensor elements for volume acquisition with significantly extended 3D FOV, which can be implemented with simple hardware and compact size. To improve image quality on the elevation plane, we implemented the synthetic aperture focusing (SAF) method according to the diagonal geometry of the virtual element array in the proposed imaging mechanism for elevation beamforming. We first evaluated the proposed imaging mechanism and SAF with simulated point targets and cyst targets. Results of point targets suggested improved image quality on the elevation plane, and results of cysts targets demonstrated a potential to improve 3D visualization of human anatomy. We built a prototype imaging system with a 3D FOV of 38 mm (lateral) by 38 mm (elevation) by 50 mm (axial) and collected data in imaging experiments with phantoms. Experimental data showed consistency with simulation results. The SAF method enhanced quantifying the cyst volume size in the breast mimicking phantom compared to without elevation beamforming. These results suggested that the proposed 3D US imaging mechanism could potentially be applied in clinical scenarios.

Corresponding author: Haichong K. Zhang. hzhang10@wpi.edu.

Index Terms—

3D ultrasound imaging; acoustic reflector; synthetic aperture focusing

I. Introduction

Due to its advantages in terms of safety, cost, portability, and high frame rate, ultrasound (US) imaging has been widely applied in disease diagnosis and image-guided surgical interventions. Compared to conventional two-dimensional (2D) US imaging, three-dimensional (3D) US imaging provides a volumetric field-of-view (FOV) and thus facilitates image evaluation and interpretation, as well as intervention planning [1–3]. By far, 3D US imaging has been applied in fields such as cardiac imaging, prostate imaging, and fetus imaging [2]. Existing options for implementing 3D US imaging include using a 2D transducer array [1] (Fig. 1(a)), a mechanically actuated one-dimensional (1D) array that conducts linear, tilting, or rotational scanning [2] (Figs. 1(b)-(c)), and sensor-tracking-free-hand scanning [3]. Although the 2D array is capable of real-time 3D imaging, it requires expansive and sophisticated hardware, making it less accessible than a mechanically actuated 1D array. Among three mechanical scanning approaches of a 1D array, tilting and rotational scanning are useful in applications like prostate cancer imaging, where a side-firing linear array transrectal US probe is tilted about an axis parallel to the transducer face to collect a fan-like volume of images [4]. However, the image quality in tilting and rotational scanning deteriorates as the distance increases with respect to the tilting or rotational axis [3]. And especially for the rotational scanning, the image quality is sensitive to operator or patient motion since acquired 2D images intersect along the axis of rotation in the center of the 3D image, and motion will cause the axial pixels to have inconsistent values in different 2D images [3]. Linear scanning, which has a relatively more homogeneous resolution, is more suitable in applications where images need to be acquired across the patient's skin, such as breast, cardiac, and tumor vascular imaging [5]. However, a linear scanning 1D array usually requires an external actuation mechanism to hold the probe and track its position, e.g., a robotic arm [6]. While using an external actuation unit provides extensive FOV and accurate tracking, actuating the 1D array probe is not trivial due to its mass and geometry. Building a dedicated probe actuation unit is costly and will increase the system's overall size. A new linear scanning solution is needed to keep the advantages of the externally actuated 1D probe, i.e., homogeneous pixel size, large FOV, adaptability to commercially available clinical probes, and at the same time be low-cost and compact.

Acoustic reflectors were first introduced to change the orientation of acoustic waves in photoacoustic (PA) imaging devices [7–10], and previous work demonstrated their capability in facilitating fast 3D US imaging by rotating the acoustic beam to cover a fan-like 3D region [11]. In the context of linear scanning, volume data can be collected by actuating the reflector only, and no mechanism is needed to move the probe. The advantage of actuating the reflector lies in the reflector's smaller size and mass compared to the probe. The size of the reflector can be minimized as long as the incident acoustic beam is covered, which indicates that an actuator with a smaller size and power can be used to make the whole imaging system more compact. We here propose a new US imaging mechanism

combining a 1D array and motor-actuated acoustic reflector to achieve 3D data acquisition in a linear scanning manner (Fig. 2(a)). A commercially available clinical 1D array is placed horizontally and faces a glass-based acoustic reflector at a 45 ° angle with respect to the axial axis of the probe. The acoustic wave is reflected by 90° and thus travels in the vertical direction. 2D slices of radio frequency (RF) data are collected as the acoustic reflector moves along the elevation direction. A variation of the proposed image mechanism includes two acoustic reflectors, with one stationary reflector and one actuated reflector (Fig. 2(b)), where the 1D array is placed vertically. An advantage of the proposed imaging mechanism over the custom 3D imaging probe is the adaptability with most of the commercially available 1D arrays. Since the actuator lies inside the imaging mechanism, size is reduced significantly and can suit hand-held operations.

In addition, RF data are beamformed on the elevation plane to improve the quality of the 3D US image. The acoustic lens elevation focal point is regarded as the virtual element to synthesize the elevation aperture information, and delay-and-sum (DAS) is applied to focus the signals. Yet, synthetic aperture focusing (SAF) should be implemented according to the diagonal geometry of the virtual element array in the proposed mechanism. This is because the proposed mechanism varies the location of the effective focal point as the distance between the transducer array and reflector changes, i.e., scatters at the same axial positions in the image space have different physical depths. Therefore, we reformulate SAF by adding a variable depth function to accommodate this unique geometry of the virtual element array.

In this paper, we present the theory of acoustic wave reflection and the adapted SAF in Section II. We discuss the validation of SAF in the proposed imaging mechanism through simulation and prototype imaging system implementation, as well as the experimental setup in Section III. Validation results are presented in Section IV, which is followed by a discussion in Section V and conclusions in Section VI.

II. Theories and Methods

This section introduces the theory of acoustic wave reflection in the proposed imaging mechanism, the 3D US data acquisition pipeline, and the SAF method aiming to improve image quality on the elevation plane.

A. Reflection of Acoustic Wave

Acoustic reflectors were proven to be able to reorient acoustic waves with minimal energy loss. Previous work [11–13] demonstrated successful acoustic reflector application in the 3D US imaging. A quantified study investigating the amount of distortion in US beam caused by acoustic reflector was carried out by Dong et al. [11]. Acoustic reflectors are usually made of materials such as glass and metal, whose acoustic impedance are significantly different from that of medium of acoustic wave propagation, like water and gel; thus, there is a high acoustic reflection coefficient on the media interface. The reflection of acoustic waves in the proposed imaging mechanism is illustrated in Fig. 3(a). Here, we examine if there is a loss of acoustic energy caused by the reflector in the proposed mechanism based on Snell's law [14]. The acoustic incidence angle θ_i is related to the refraction angle θ_r as described in (1):

$$\frac{\sin(\theta_i)}{\sin(\theta_r)} = \frac{c_1}{c_2} \tag{1}$$

The acoustic wave propagates from Medium 1 (speed of sound is c_1) into Medium 2 (speed of sound is c_2). Although only longitudinal wave approaches the media interface, there can be both longitudinal and shear waves transmitting into Medium 2. Speeds of longitudinal and shear waves in Medium 2 are denoted as c_{2d} and c_{2s}, respectively. The first critical condition occurs when the refraction angle of the longitudinal wave becomes 90°, and the corresponding incident angle is defined as the first critical angle θ_{c1}, as in (2). If $\theta_i > \theta_{c1}$, no longitudinal wave transmits through the interface.

$$\theta_{c1} = \text{asin}\left(\frac{c_1}{c_{2d}}\right) \tag{2}$$

The second critical condition occurs when the refraction angle of shear wave becomes 90°, and the corresponding angle is defined as the second critical angle θ_{c2},

$$\theta_{c2} = \text{asin}\left(\frac{c_1}{c_{2s}}\right) \tag{3}$$

If $\theta_i > \theta_{c2}$, all acoustic energy that arrives on the media interface will be reflected. In this work, the acoustic reflector is made of glass and immersed in water. Given these conditions, c_1, c_{2d}, c_{2s} are assumed to be 1480 m/s, 5100 m/s, 2840 m/s, respectively [15]. It could be easily computed using (2) and (3) that $\theta_{c1} \cong 16.87$ ° and $\theta_{c2} \cong 31.41$ °. Since the incident angle is 45 ° in the proposed imaging mechanism (larger than both critical angles), there will be no loss in acoustic energy in acoustic reflection theoretically.

B. 3D US Data Acquisition

The actuated reflector scans with fixed step size, and thus location information of each acquired RF slice is available. After beamforming on the lateral plane, RF slices are stacked and beamformed on the elevation plane, and such two-step beamforming is illustrated in Fig. 3(b).

C. Adaptation of Synthetic Aperture Focusing (SAF)

To improve image quality on the elevation plane, we implement the SAF method. Nikolov and Jensen [16] first applied synthetic aperture focusing (SAF) based on the concept of virtual element for elevation beamforming in a 3D US imaging system, which is implemented with the linearly translated 1D array. In the proposed imaging mechanism, distance from the probe to the reflector is variable, resulting in a changing physical depth in received signals from scatters with the same axial position in the image space. Hence, an adapted version of the SAF method incorporating the varying elevation focal point is needed.

In the linearly translated 1D array, the trajectory of a single elevation focal point forms a virtual element array parallel to the scanning direction, as shown in Fig. 3(c). In contrast, the virtual element array of the proposed imaging mechanism is diagonal with respect to the scanning direction of the reflector, as shown in Fig. 3(d): on each acquisition position, the virtual element is found using the mirror-reflection symmetry. The SAF method is reformulated based on the geometry of the virtual element array in the proposed imaging mechanism, as summarized in (4)-(8). Since only signals from the space below the reflector include echoes from the imaging subject, the RF data received at step n, or RF_n, are time-delayed by the amount of d_{comp} to compensate for path-length differences as formulated in (4)-(5),

$$d_{comp}(n) = d_{tr,m} + n * \Delta\delta + d_{m,int} \tag{4}$$

$$RF'_n(t) = RF_n\left(t + \frac{2d_{comp}(n)}{c_{in}}\right) \tag{5}$$

where $d_{tr,m}$ represents the distance from the surface of the US transducer (denoted as tr) to the acoustic reflector (denoted as m) when the reflector is in the home position, $d_{m,int}$ represents the distance from the reflector to the interface, which separates the space inside the imaging device from the outside, t is the time of flight, c_{in} is the speed of sound inside the device, and $\Delta\delta$ is the step size of the linear motion. The time-delayed data, RF'_n, are beamformed on the elevation plane using DAS. The beamformed RF data, RF_{DAS}, is formulated in (6).

$$RF_{DAS}(z_i, y_i) = \sum_{n=1}^{N_p} RF'_n(t_d(y_n, z_i, y_i, n)) \tag{6}$$

where z_i and y_i are locations of a particular pixel i in the axial direction and the elevation direction, respectively. The time delay between the location of pixel i and the virtual element with elevation location y_n is denoted as t_d, being computed as (7) and (8).

$$SS = \frac{C_{out}}{2f_s} \tag{7}$$

$$t_d(y_n, z_i, y_i, n) = \frac{2\left(\sqrt{((y_i - y_n) * \Delta\delta)^2 + \left(z_i * ss + d_{comp}(n) - F\right)^2} - d_{comp}(n)\right)}{c_{out}} \tag{8}$$

In (7), ss is the axial sampling spacing, c_{out} is the speed of sound outside of the imaging device (since the speed of sound inside and outside of the imaging can be different in real applications), f_s is the sampling frequency. In (8), F is the elevation focal depth. Since the RF data are time-delayed in (5), the amount of depth compensation d_{comp} needs to be considered when computing time delays. Coherent factor (CF) is optionally used as a non-linear weighting function in DAS to enhance image visibility. (9) and (10) show the implementation of CF.

$$CF(z_i, y_i) = \frac{\left|\sum_{n=1}^{N_p} RF'_n(t_d(y_n, z_i, y_i, n))\right|^2}{N_p * \sum_{n=1}^{N_p} |RF'_n(t_d(y_n, z_i, y_i, n))|^2} \quad (9)$$

$$RF_{DAS+CF}(z_i, y_i) = CF(z_i, y_i) * RF_{DAS}(z_i, y_i) \quad (10)$$

III. Implementation

This section provides implementation details of simulation studies, optimization of imaging parameters such as motion step size and central frequency, and the setup for imaging experiments conducted to validate the SAF method.

A. Simulation Setup

Simulation studies were implemented in MATLAB with the Field II simulation platform [17] to validate the SAF method. A model of ATL L12-5 38 mm linear array was set up in the simulation (the same probe was used for the experiment). The central frequency was configured to be 5 MHz, and the sampling frequency was 40 MHz. The linear motion step size was set as 200 μm with a scanning range of 38 mm. The elevation and axial locations of imaging targets were adjusted to simulate the varying length of the acoustic path on each acquisition position. In addition, a 10 dB white noise (with respect to the measured power of RF data) was added to RF data. Point targets were used to evaluate the point spread function (PSF) of the 3D US imaging system, and a phantom of three cysts (the diameter of every cyst was 10 mm) was used to investigate the potential in imaging human anatomy. Key parameters for the simulation study setup are summarized in Table 1. In DAS, a constant f-number of 0.1 was used to guarantee consistent resolution along the axial direction.

B. System Optimization and Tolerance Evaluation

Point targets simulation was used for imaging parameter optimization [23] as well. In this paper, the central frequency f_0 and the elevation motion step size $\Delta\sigma$ were varied to investigate their effects on the image quality. In the central frequency study, the elevation motion step size was kept as 200 μm, and the central frequency was changed from 1 MHz to 10 MHz; while in the motion step size study, the central frequency was fixed at 5 MHz, and the elevation motion step size was changed from 200μm to 1800 μm.

C. Experiment Setup

The prototype 3D US imager and imaging system are shown in Fig. 4 and Fig. 5, where the data acquisition platform (Vantage 128, Verasonics Inc., WA, USA) sent motion command to the actuator (NEMA 14 non-captive stepper motor, PCB Linear, IL, USA) via serial port after data acquisition on each sampling position. The linear motion step size was 200 μm, and the maximum elevation scan was 38 mm. The linear array (ATL L12-5 38mm) was configured to emit plane-wave [18] at 7 different angles evenly spaced in the range of −18° and +18°. The size of the glass-based actuated reflector (Edmund Optics, NJ, USA) was 50 mm (length, parallel to the lateral direction of the linear array) by 25 mm (width).

The central frequency of the linear array was 7.8 MHz, the sampling frequency was 31.24 MHz, and the pulse repetition frequency was 4.5 KHz. Two apertures were activated for transmitting and receiving. The first aperture consisted of elements no.1 to no.128, and the second aperture consisted of elements no.65 to no.192. RF data were beamformed on the lateral plane using the embedded program on the data acquisition platform. Two types of phantoms were scanned: fishing-wire phantom (Nylon, 200 μm diameter) and breast elastography phantom (Part Number 1552-01, CIRS), aiming to evaluate the PSF and human tissue imaging potential of the prototype. The prototype imager was supported by a metal frame and fixed on top of a water bath. Phantoms and the part of the prototype were submerged in the water tank, including a 1D array and actuated acoustic reflector.

D. Calibration of Acoustic Path with Optical Method

The ideal angle of the acoustic reflector with respect to the acoustic path is 45 °; however, the actual angle might have an error due to 3D printing and installation. Calibration was carried out to validate if the angle matched the ideal value. A laser level was used to visualize the acoustic path by orienting the laser beam towards the reflector, and the reflected beam landed on the acoustic lens of the US probe, as shown in Fig. 6 (a). The beam landing position on the transducer was used to verify if an error exists in the reflector angle. If the beam landing location changes as the reflector moves, it means that an error exists in the reflector angle. The reflector was moved to four different locations, and the averaged offset was found as 2.52 mm with a standard deviation of 0.08 mm. Since the beam landing location was consistent when the reflector was placed in different elevation positions, we concluded that the error in the reflector angle was minimized.

IV. Results

Simulated data were used to evaluate the effects of SAF on improving image quality on the elevation plane. Experimental data showed consistency with simulation results in both cases of point targets and the breast elastography phantom.

A. Simulated Points and Cysts

In the simulation with point targets, elevation images in the central lateral position with and without SAF are displayed in Figs. 7(a), (d) with 40 dB dynamic range. The point target at 27 mm depth is chosen for further examination, whose contour plots are shown in Figs. 7(b), (e). The quality of elevation images is evaluated with the full width at half maximum (FWHM) and the signal-to-noise ratio (SNR). PSF in 3D space is segmented at −20dB and visualized in Figs. 7(c), (f) to illustrate the improvement in 3D image resolution. In the simulation with cysts phantom, images on the central lateral position are displayed in Fig. 8 with 60 dB dynamic range to demonstrate the potential of SAF in improving the image quality of human anatomy. Contrast-to-noise ratio (CNR) [21–22] is computed to evaluate the change of image quality after applying SAF. The formula of CNR is given in (11),

$$CNR = \frac{|\mu_1 - \mu_2|}{\sqrt{\sigma_1{}^2 + \sigma_2{}^2}} \tag{11}$$

where μ_1 and μ_2 are mean pixel values of ROI and background region, and σ_1^2 and σ_2^2 are corresponding standard deviation values.

B. System Optimization and Tolerance Evaluation

Different combinations of motion step size and central frequency were experimented with simulations, FWHM and SNR were used as criteria to evaluate the image quality from each combination. In the case of step size study, images were interpolated in the elevation direction for the convenience of quantification. The central frequency study (Figs. 9(a), (c)) suggests using a higher central frequency could benefit both the resolution and SNR. Also, the trend in the step size study (Figs. 9(b), (d)) suggests an upper limit for step size around 1000 μm, above which the spatial sampling along the elevation direction is insufficient. Such a phenomenon is explained by the upper limit of the elevation sampling step for a synthetic aperture system based on a single, circular transducer, as introduced in [24]. We assume that the elevation beam pattern of elements in a linear array is equivalent to that of a single circular element whose diameter equals the height of elements in the linear array, and the upper limit of the step size in the proposed system can be defined, as shown in (12). Since the element height h was set to be 4.5 mm, the motion step size should be smaller than 1125 μm (1/4 of 4.5 mm), and according to the step size study results, a small step size brings better resolution after applying SAF. As a result, in experiments, the central frequency was chosen as 7.81 MHz, and the elevation step size was chosen as 200 μm.

$$\Delta\delta \leq \frac{h}{4} \tag{12}$$

C. Wires Phantom

In the wires phantom imaging experiment, a phantom of four fishing wires was scanned with wires aligned with the lateral direction of the probe to simulate point targets on the elevation plane. With and without SAF images on the central lateral position are shown in Figs. 10(a), (c), displayed with a 40 dB dynamic range. The visualized volume data of wires segmented at −20 dB are presented in Figs. 10(b), (d). The displayed FOV is 38 mm (lateral) by 38 mm (elevation) by 25 mm (axial). FWHM and SNR of four wire targets were computed and summarized in Table 3.

D. Breast Phantom

A breast elastography phantom with cystic masses was imaged in this experiment. One of the cystic masses was chosen as the imaging target, and its neighboring region was scanned. Images on the elevation plane are visualized in Fig. 11 for both with and without SAF cases with a 70 dB dynamic range. 3D US data of the scanned volume are visualized in Fig. 13, with the cyst located in the central location. MRI scanning of the breast phantom was conducted to evaluate the performance of SAF on the breast phantom data. The diameter of the cyst in the breast phantom was estimated according to segmented MRI cyst volume and was referred to as the ground truth to compare with the cyst diameter estimated from the US volume. The cyst region in MRI image was segmented using the level tracing function in 3D Slicer [25], and then the diameter of the cyst was computed based on the volume of the cyst

(assumed to be a sphere), which turned out to be 7.14 mm. MRI images of the cyst in breast phantom and segmented cyst volume are demonstrated in Figs. 12 (a)-(b). The CNR between the cyst region and the background was computed for with and without SAF images, and the cyst's diameter was measured from US images (as shown in Figs. 12 (c)-(e)) and compared with the ground truth value estimated from MRI image, as summarized in Table 4.

V. Discussion

We validated the proposed 3D US imaging mechanism for its capability in obtaining volume data and improved image quality on the elevation plane, benefiting from the SAF method adapted to the proposed imaging mechanism in both simulations and experiments. We demonstrated that the proposed imaging mechanism could adapt to a clinically available probe and does not require dedicated probe design and fabrication like existing 3D US imaging systems. The range of the reflector motion can be adjusted to fit the requirement of different imaging applications. Since the mass of the reflector is smaller than a probe (the mass ratio between reflector and probe is 1:15), a higher volume rate is potentially achievable compared to actuating the 1D array linearly. Such a reflector-based imaging mechanism could also be valuable in US image-guided needle intervention [29–31] by opening a hole on the reflector to allow the needle to pass [32]. In this way, the needle path is registered to the image plane to provide stable visualization of the needle during the insertion process.

The concept of treating the transducer focal point as a virtual element in SAF was first introduced by Passman and Ermert [33] to overcome the limitation in lateral resolution in traditional B-mode imaging [34]. With the successful demonstration of its applicability in improving image quality on the elevation plane of the linearly translated 1D array [16], SAF has been applied in various forms of 3D US imaging systems, including a rotated phased array probe [35] and robot-tracked convex probe [6] to improve 3D data quality. This paper further demonstrates the applicability of SAF in the variable virtual point settings. In the conventional 1D array elevation translation, virtual elements have the same depths, while in the proposed reflector-integrated elevation translation, virtual elements have different depths, leading to twofold effects. First, the depth-dependent attenuation is inhomogeneous along the elevation direction. Depth-dependent attenuation grows as the reflector moves away from the transducer. Second, the PSF changes along the elevation direction because the elevation beamwidth is also depth-dependent. As a result, the resolution deteriorates as the reflector moves to the far side of FOV. A phenomenological model [14] in (13)-(14) is used in plotting the attenuation as a function of depth in physical space to evaluate the change in depth-dependent attenuation along the elevation direction in the image space,

$$\frac{A_z}{A_0} = \exp(-\mu_a * z) \tag{13}$$

$$loss_{dB}(z) = 20\log(\exp(-\mu_a * z)) \tag{14}$$

where A_0 is the amplitude of the acoustic signal at depth 0, A_z is the amplitude of the acoustic signal at depth z. μ_a is the amplitude attenuation factor, depending on the

transducer's central frequency and medium. In our experiments, the central frequency was 7.8 MHz, and the medium was water, resulting in μ_a of 1.54 Np/m. By finding the corresponding range of depth in the physical space of 25mm depth in the image space, the difference between attenuation as the reflector scans across the FOV can be found, which is 0.51 dB. Although the attenuation difference is relatively small, we can compensate it by applying a weighting factor, as shown in (15), where A'_z is the ultrasonic signal amplitube after compensation.

$$A'_z = \frac{A_z}{\exp(-\mu_a * z)} \tag{15}$$

As mentioned earlier, elevation resolution in the image space is inhomogeneous in the proposed imaging mechanism. However, we use a fixed f-number in DAS beamforming which results in constant elevation resolution at all depths, mitigating the resolution deterioration. To further evaluate to what extent resolution deterioration could happen and how it is mitigated by using a fixed f-number in beamforming, we conducted another simulation where seven-point targets were placed at the same depth (25 mm) but horizontally at different elevation locations. The corresponding parameters were used in the simulation, as presented in Table 1, while a central frequency of 7.8 MHz was used. We also simulated the case where the linear array was directly translated in the elevation direction to collect 3D data, and the conventional SAF was applied. From obtained results, the deterioration of resolution along the elevation direction is observed in the proposed image mechanism, while the resolution is constant in a translated 1D array before applying elevation beamforming. After applying SAF with a fixed f-number, equivalent resolutions of the 1D array elevation translation and the proposed reflector-integrated elevation translation are achieved. Fig. 15 shows the FWHM of seven-point targets in both translation settings.

Due to the existence of the acoustic reflector, the US probe cannot get in direct contact with the patient. The imaging device needs to be emersed in the acoustic medium (water or ultrasound gel) and encapsulated. However, the interface of the encapsulation can attenuate acoustic energy and cause multiple reflection artifacts on US images. Previous work using acoustic reflectors for hand-held PA/US imaging also reported similar issues that are not yet solved [9–11]. Potential encapsulation of the proposed imaging mechanism can be built by referring to encapsulations used in mechanically swept a 3D US probe [3] or automated breast ultrasound imaging system (Invenia ABUS 2.0, General Electric Healthcare) [26]. Materials with similar acoustic impedance to water can be used for the interface layer [27] to minimize multiple reflection artifacts. Also, advanced signal processing methods are helpful in removing multiple reflection artifacts [28]. Such an encapsulation solution can be generalized and will benefit other imaging mechanisms involving acoustic reflectors.

Volume rate is another limitation of the prototype. The current scanning time for the volume data is around 1.5 minutes, with 0.5 seconds pause between every two steps in linear scanning to ensure accurate acoustic reflector positioning, limiting the 3D imaging frame rate. Approaches to improve volume rate include using a linear actuator with higher motion speed, such as piezo linear motors, and enabling continuous scanning without pausing

between steps. Also, the interaction between the moving reflector and acoustic medium should be considered. If the ultrasonic gel is used as the medium, the viscosity of the gel may limit scanning speed; if water is used as the medium, inducing water flow may affect US signals when the reflector moves at high speed.

The prototype currently has a size of 315 mm (length) by 135 mm (width) by 85 mm (height), which can be cumbersome for hand-held use. The design of the encapsulation tank can be optimized to encompass only part of the probe that is submerged in an acoustic medium. There are other approaches to improve the size, like using a smaller actuator and minimizing the 3D printed components. Additionally, *in-vivo* experiments need to be conducted to study the effects of tissue and motion of subjects on the performance of the proposed imaging mechanism.

In comparison with a rotating reflector [7], [11], although the proposed imaging mechanism cannot achieve the same volume rate yet, it provides a larger FOV and more homogeneous image resolution, especially along the axial direction on the elevation plane. The same elevation beamforming as proposed in this paper can be applied in a rotating reflector. However, it is worth noting that the effective aperture size in the rotating reflector is not increased, and thus the impact of applying elevation beamforming would be limited.

VI. Conclusions

In this paper, we proposed a mechanism based on actuated acoustic reflector for 3D US imaging to overcome the limitations in conventional 3D US imaging systems. Unlike a 2D array, the proposed mechanism requires only simple hardware and enjoys lower cost. At the same time, it has a larger FOV compared to a hand-held integrated 1D array and does not require an external actuation unit. The SAF beamforming method is implemented according to the diagonal geometry of the virtual element array in the proposed imaging mechanism to improve the quality of the 3D US image on the elevation plane. Results from the simulation demonstrated that SAF improves image quality on the elevation plane by achieving lower FWHM and higher SNR. The prototype of the imaging mechanism was built with 38mm (lateral) by 38mm (elevation) by 50mm (axial) FOV and was used to scan the fishing-wire phantom and breast phantom. Results from experiments were consistent with simulation studies, providing further validation to the proposed imaging mechanism in its 3D imaging capability and improved image quality on the elevation plane brought by SAF. For future work, we will put emphasis on developing an effective encapsulation for the proposed imaging mechanism and improving its scanning speed to pave the way toward clinical applications.

Acknowledgments

The authors would like to acknowledge Mr. Enxhi for his help with manufacturing the metal support frame in the experimental setup and Mr. Shang Gao for his help with delay-and-sum and coherent factor implementation.

This work was supported in part by Worcester Polytechnic Institute internal fund; in part by the National Institute of Health under Grant DP5OD028162, R01CA134675.

Biographies

Yichuan Tang received BEng with honours in Mechanical Engineering from the University of Nottingham (China campus), Ningbo, 2016. He received MS in Robotics Engineering from Johns Hopkins University in 2018. Since 2019 he has been a PhD student in the department of Robotics Engineering in Worcester Polytechnic Institute, Worcester, MA, USA. His research focuses on ultrasound and photoacoustic imaging instrumentation. He is affiliated with Medical FUSION Lab directed by Dr. Haichong K. Zhang.

Ryosuke Tsumura (M'17) received his BS, MS and PhD in Mechanical Engineering from Waseda University, Tokyo, Japan in 2014, 2016 and 2019, respectively. He is currently a researcher in the Health and Medical Research Institute at the National Institute of Advanced Industrial Science and Technology and an affiliated postdoctoral fellow in Department of Robotics Engineering at the Worcester Polytechnic Institute, MA, USA. His current research interests include robotic intervention and ultrasound imaging.

Jakub Tomasz Kaminski was born in Poznan, Poland in 1992. He obtained BSc in Mechatronics (2016) and MS in Automatic Control and Robotics (2018) from the Poznan University of Technology, Poland. He is a MS student in the department of Robotics Engineering at Worcester Polytechnic Institute, MA, USA which he joined as a Fulbright Graduate Student Award recipient. Jakub is affiliated with Medical FUSION Lab lead by Dr. Haichong K. Zhang.

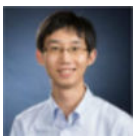

Haichong (Kai) Zhang is an Assistant Professor in Biomedical Engineering and Robotics Engineering with an appointment in Computer Science at Worcester Polytechnic Institute

(WPI). He is the founding director of the Medical Frontier Ultrasound Imaging and Robotic Instrumentation (Medical FUSION) Laboratory. The research in his lab focuses on the interface of medical imaging, sensing, and robotics, developing robotic assisted imaging systems as well as image-guided robotic interventional platforms, where ultrasound and photoacoustic imaging are two key modalities to be investigated and integrated with robotics. Dr. Zhang received his B.S. and M.S. in Human Health Sciences from Kyoto University, Japan, and subsequently earned his M.S. and Ph.D. in Computer Science from the Johns Hopkins University.

References

[1]. Smith SW, Lee W, Light ED, Yen JT, Wolf P and Idriss S, “Two dimensional arrays for 3-D ultrasound imaging,” 2002 IEEE Ultrasonics Symposium, pp. 1545–1553, Apr. 2002.

[2]. Fenster A, Downey DB, Cardinal HN, “Three-dimensional ultrasound imaging,” Phys. Med. Biol, vol. 46, no. 5, pp. 67–99, 2001.

[3]. Huang Q and Zeng Z, “A review on real-time 3D ultrasound imaging technology,” Biomed. Research Int, Vol. 2017, ID 6027029, 2017.

[4]. Downey DB and Fenster A, “Three-dimensional power Doppler detection of prostatic cancer,” Am. J. Roentgenol, vol. 165, no. 3, pp. 741, 1995.

[5]. Downey DB and Fenster A, “Vascular imaging with a three-dimensional power Doppler system,” Am. J. Roentgenol, vol. 165, no. 3, pp. 665–668, 1995. [PubMed: 7645492]

[6]. Zhang HK, Fang TY, Finocchi R, and Boctor EM, “High resolution three-dimensional robotic synthetic tracked aperture ultrasound imaging,” Proc. SPIE 10139, Medical Imaging 2017: Ultrasonic Imaging and Tomography, Mar. 2017.

[7]. Huang C, Yao J, Wang LV, and Zou J, “A water-immersible 2-axis scanning mirror microsystem for ultrasound andha photoacoustic microscopic imaging applications,” Microsyst. Technol, no. 19, pp. 577–582, Apr. 2013. [PubMed: 33867690]

[8]. Wang Y, Lim RSA, Zhang H, Nyayapathi N, Oh KW, and Xia J, “Optimizing the light delivery of linear-array-based photoacoustic systems by double acoustic reflectors,” Sci. Rep, vol. 8, no. 1, pp. 13004, Aug. 2018. [PubMed: 30158556]

[9]. Baik JW, Kim JY, Cho S, Choi S, Kim J, and Kim C, “Super Wide-Field Photoacoustic Microscopy of Animals and Humans In Vivo,” IEEE Trans. Med. Imag, vol. 39, no. 4, pp. 975–984, Apr. 2020.

[10]. Cheng Z, Wu L, Qiu T, Duan Y, Qin H, Hu J, and Yang S, “An excitation-reception collinear probe for ultrasonic, photoacoustic, and thermoacoustic tri-modal volumetric imaging,” IEEE Trans. Med. Imag, vol. 40, no. 12, pp. 3498–3506, June. 2021.

[11]. Dong Z, Li S, Lowerison MR, Pan J, Zou J, and Song P, “Fast Acoustic Steering via Tilting Electromechanical Reflectors (FASTER): A Novel Method for High Volume Rate 3-D Ultrasound Imaging,” IEEE Transactions on Ultrasonics, Ferroelectrics, and Frequency Control, vol. 68, no. 3, pp. 675–687, Sept. 2021. [PubMed: 32870789]

[12]. Tsumura R, Tang Y, and Zhang HK, “Reflector-based transrectal 3D ultrasound imaging system for transperineal needle insertion,” IEEE International Ultrasound Symposium, pp. 1–4, Sept. 2020.

[13]. Tang Y, Malik A, and Zhang HK, “Acoustic reflector-based three-dimensional ultrasound imaging,” Proc. SPIE 11602, Medical Imaging 2021: Ultrasonic Imaging and Tomography, Feb. 2021.

[14]. Prince JL and Links JM, Medical Imaging Signals and Systems, Pearson, 2015.

[15]. Selfridge AR, “Approximate material properties in isotropic materials,” IEEE Transactions on Sonics and Ultrasonics, vol. 32, no. 3, pp. 381–394, May. 1985.

[16]. Nikolov SI and Jensen JA, “3D synthetic aperture imaging using a virtual source element in the elevation plane,” IEEE International Ultrasound Symposium, vol. 2, pp. 1743–1747, Oct. 2000.

[17]. Jensen JA, “Simulation of advanced ultrasound system using Field II,” IEEE International Symposium on Biomedical Imaging, vol. 1, pp. 636–639, Apr. 2004.

[18]. Montaldo G, Tanter M, Bercoff J, Benech N, and Fink M, “Coherent plane wave compounding for very high frame rate ultrasonography and transient elastography,” IEEE Transactions on Ultrasonics, Ferroelectrics, and Frequency Control, vol. 56, no. 3, pp. 489–506, Mar. 2009. [PubMed: 19411209]

[19]. Jeon S, Park E, Choi W, Managuli R, Lee K, and Kim C, “Real-time delay-multiply-and-sum beamforming with coherent factor for in vivo clinical photoacoustic imaging of humans,” Photoacoustics, vol. 15, Sept. 2019.

[20]. Mozaffarzadeh M, Yan Y, Mehrmohammadi M, and Makkiabadi B, “Enhanced linear-array photoacoustic beamforming using modified coherence factor,” J. Biomed. Opt, vol. 23, no. 2, Feb. 2018.

[21]. Timischl F, “The Contrast-to-Noise Ratio for Image Quality Evaluation in Scanning Electron Microscopy,” SCANNING, vol. 37, pp. 54–62, Jan. 2015. [PubMed: 25533747]

[22]. Kempski KM, Graham MT, Gubbi MR, Palmer T, and Bell MAL, “Application of the generalized contrast-to-noise ratio to access photoacoustic image quality,” Biomedical Optics Express, vol. 11, no. 7, pp. 3684–3698, July. 2020. [PubMed: 33014560]

[23]. Moshavegh R, Jensen J Sr., Villagomez-Hoyos CA, Stuart MB, Hemmsen MC, and Jensen JA, “Optimization of synthetic aperture image quality,” Proc. SPIE 9790, Medical Imaging 2016: Ultrasonic Imaging and Tomography, Apr. 2016.

[24]. Stepinski T, “Synthetic aperture focusing technique in ultrasound inspection of coarse grained materials,” Swedish Nuclear Power Inspectorate Report 2008:06, Dec. 2007.

[25]. Pinter Cs., Lasso A, Fichtinger G, “Polymorph Segmentation representation for medical image computing,” Computer Methods and Programs in Biomedicine, Vol. 171, pp. 19–26, Apr. 2019. [PubMed: 30902247]

[26]. Vaughan CL, “Novel imaging approaches to screen for breast cancer: Recent advances and future prospects,” Medical Engineering & Physics, vol 72, pp. 27–37, 2019. [PubMed: 31554573]

[27]. Guillermic RM, Lanoy M, Strybulevych A, Page JH, “A PDMS-based broadband acoustic impedance matched material for underwater applications,” Ultrasonics, vol. 94, pp. 152–157, Apr. 2019. [PubMed: 30322641]

[28]. Lambert W, Cobus LA, Frappart T, Fink M, and Aubry A, “Distortion matrix approach for ultrasound imaging of random scattering media,” PNAS, vol. 117, no. 26, pp. 14645–14656, June. 2020. [PubMed: 32522873]

[29]. Zhang HK, Kim Y, Lin M, Paredes M, Kannan K, Moghekar A, Durr NJ and Boctor EM, “Toward dynamic lumber puncture guidance using needle-based single-element ultrasound imaging,” J. Med. Imaging, vol. 5, no. 2, Apr. 2018.

[30]. Tsumura R, Vang DP, Hata N, and Zhang HK, “Ring-arrayed forward-viewing ultrasound imaging system: a feasibility study,” Proc. SPIE 11319, Medical Imaging 2020: Ultrasonic Imaging and Tomography, Mar. 2020.

[31]. Tsumura R and Zhang HK, “Forward-viewing ultrasound imaging with concentric-ring arrays for registration-free needle intervention,” IEEE International Ultrasound Symposium, pp. 1–4, Sept. 2020.

[32]. Tang Y, Abouaf I, Malik A, Tsumura R, Kaminski JT, Sorokin I, Zhang HK, “Mirror-Integrated ultrasound image-guided needle access,” Proc. SPIE 12034, Medical Imaging 2022: Image-Guided Procedures, Robotics Interventions and Modelling, Feb. 2022.

[33]. Passman C and Ermert H, “A 100-MHz ultrasound imaging system for dermatologic and ophthalmologic diagnostics,” IEEE Transactions on Ultrasonics, Ferroelectrics, and Frequency Control, vol. 43, no. 4, pp. 545–552, July. 1996.

[34]. Frazier CH and O’Brien WD, “Synthetic aperture techniques with a virtual source element,” IEEE Transactions on Ultrasonics, Ferroelectrics, and Frequency Control, vol. 45, no. 1, pp. 196–207, Jan. 1998. [PubMed: 18244172]

[35]. Nikolov SI, Jensen JA, Dufait R, and Schoisswohl A, “Three-dimensional real-time synthetic aperture imaging using a rotating phased array transducer,” IEEE Ultrasonics Symposium, vol. 2, pp. 1585–1588, Oct. 2002.

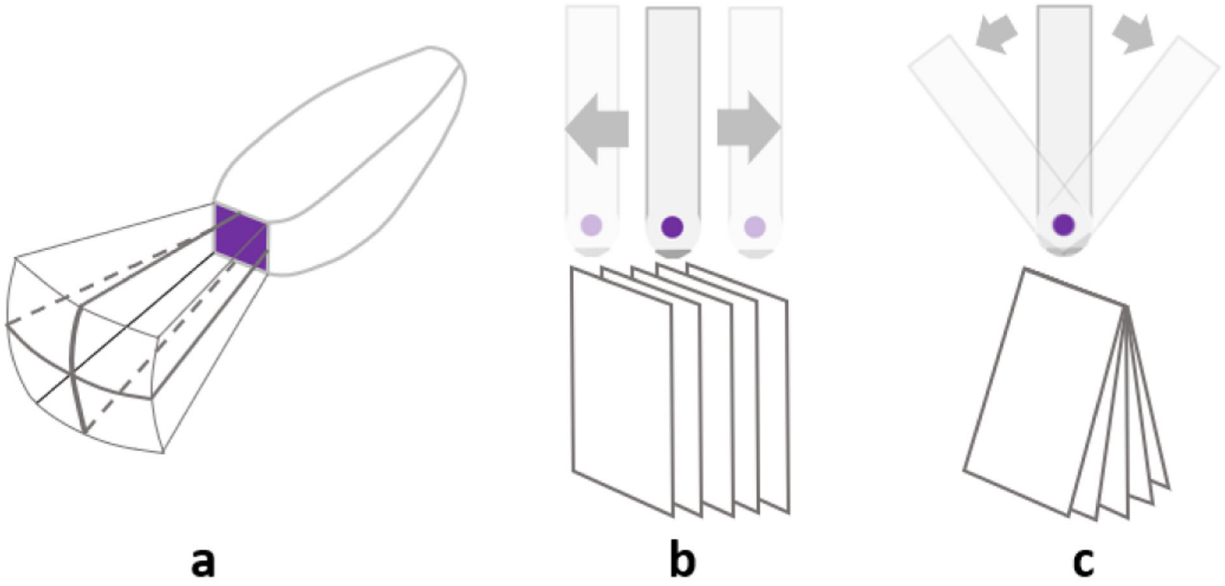

Fig. 1. Conventional approaches to implement 3D US imaging.

(a) 2D array transducer. (b) 1D array with linear scanning. (c) 1D array with tilting scanning.

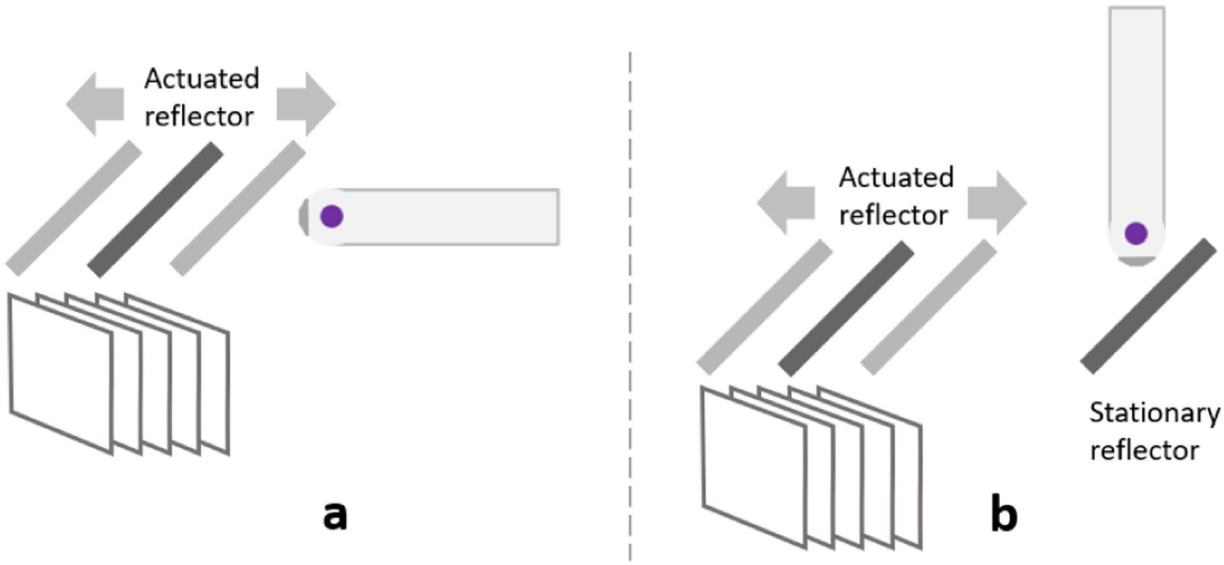

Fig. 2. Proposed approaches to implement 3D US imaging using actuated acoustic reflectors.
(a) 1D array with a single actuated acoustic reflector for linear scanning. (b) 1D array with two acoustic reflectors, one stationary and one actuated for linear scanning.

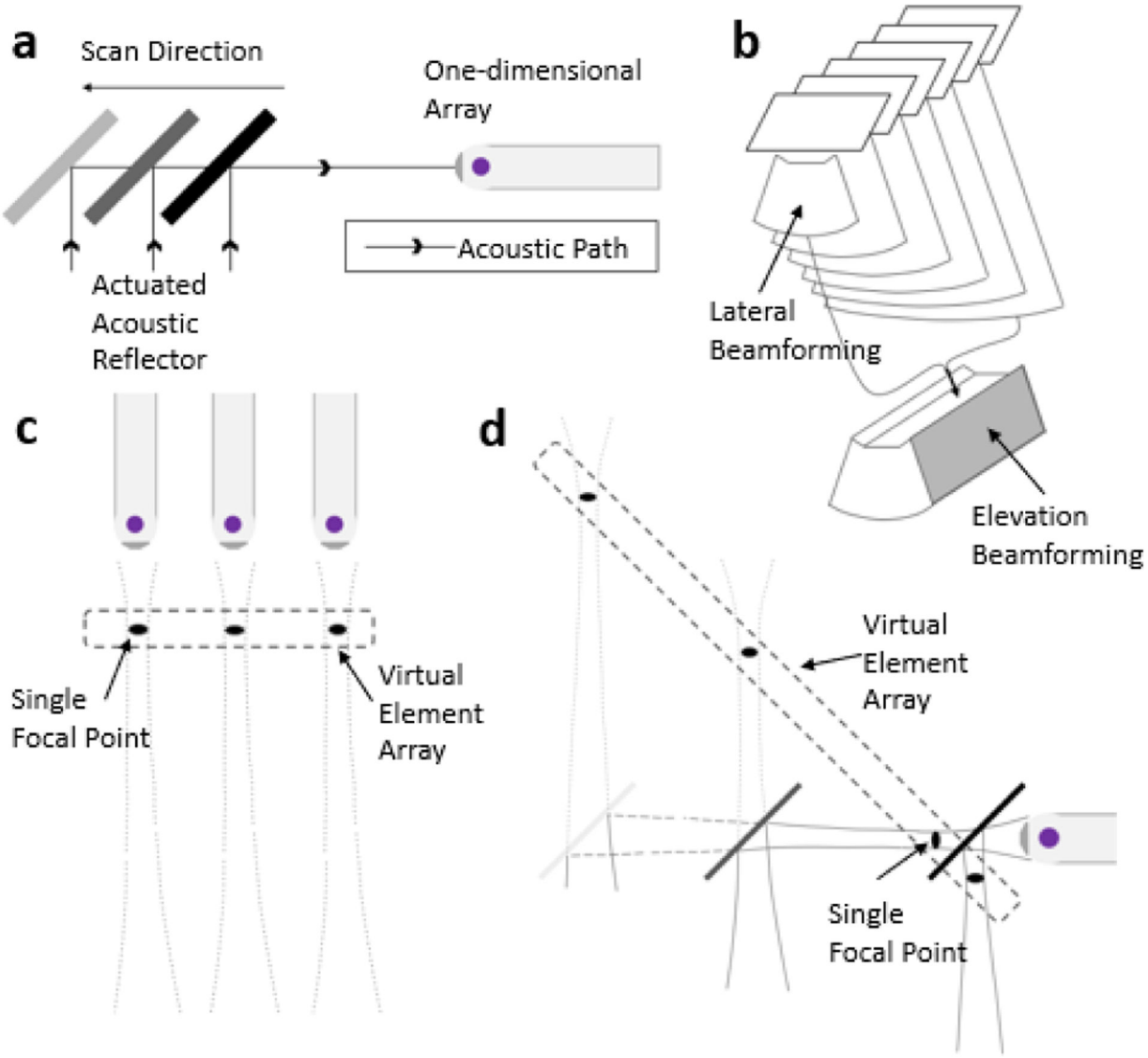

Fig. 3. 3D US image data acquisition and the SAF method.

(a) Acoustic path with actuated reflector. (b) Two-steps beamforming. (c) Virtual element array in linear scanning 1D array (parallel to the scanning direction). (d) Virtual element array in proposed imaging mechanism (diagonal with respect to the scanning direction).

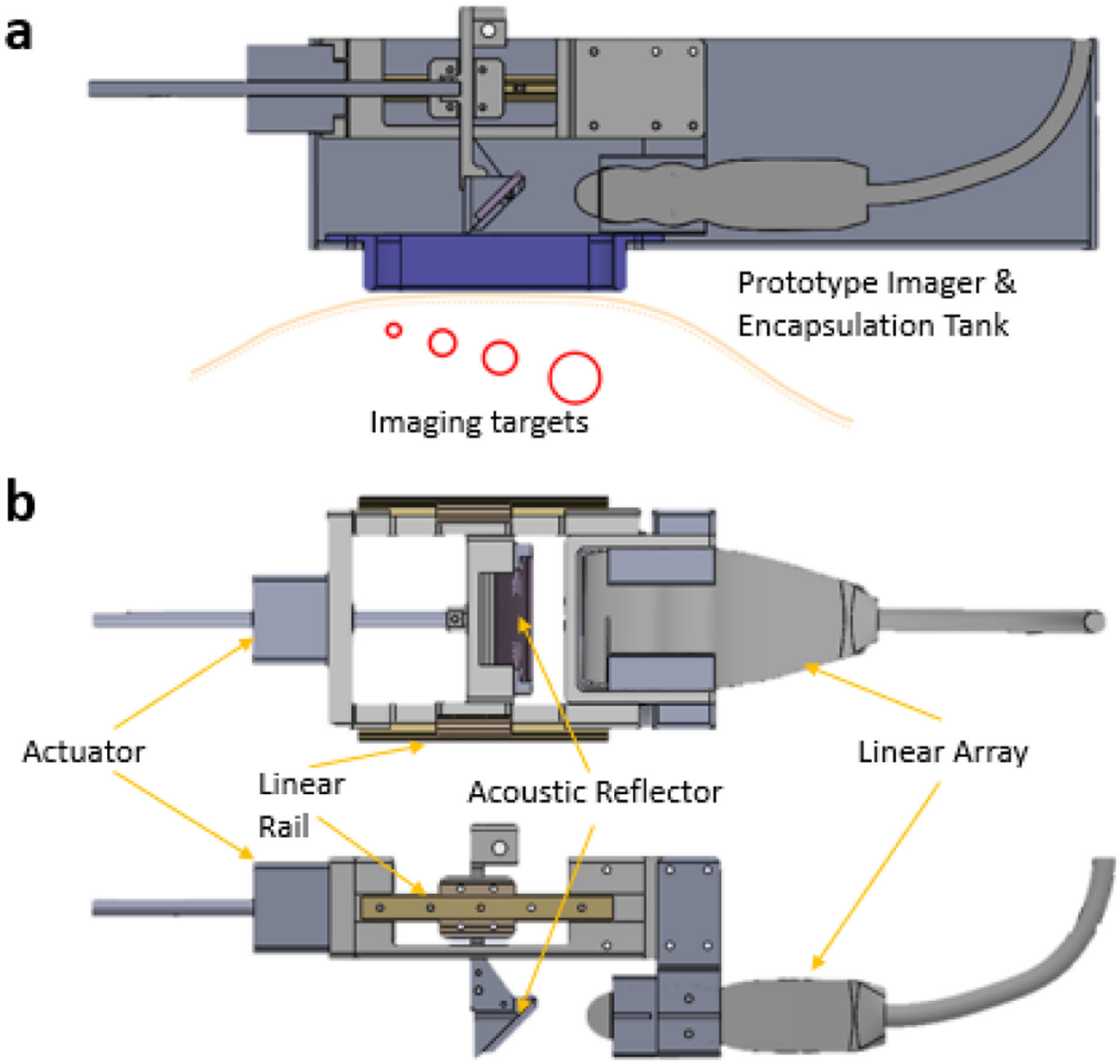

Fig. 4. Prototype 3D US imager based on a single actuated acoustic reflector.

(a) Concept of prototype imager inside encapsulation water tank scanning targets. (b) Design details of the prototype imager.

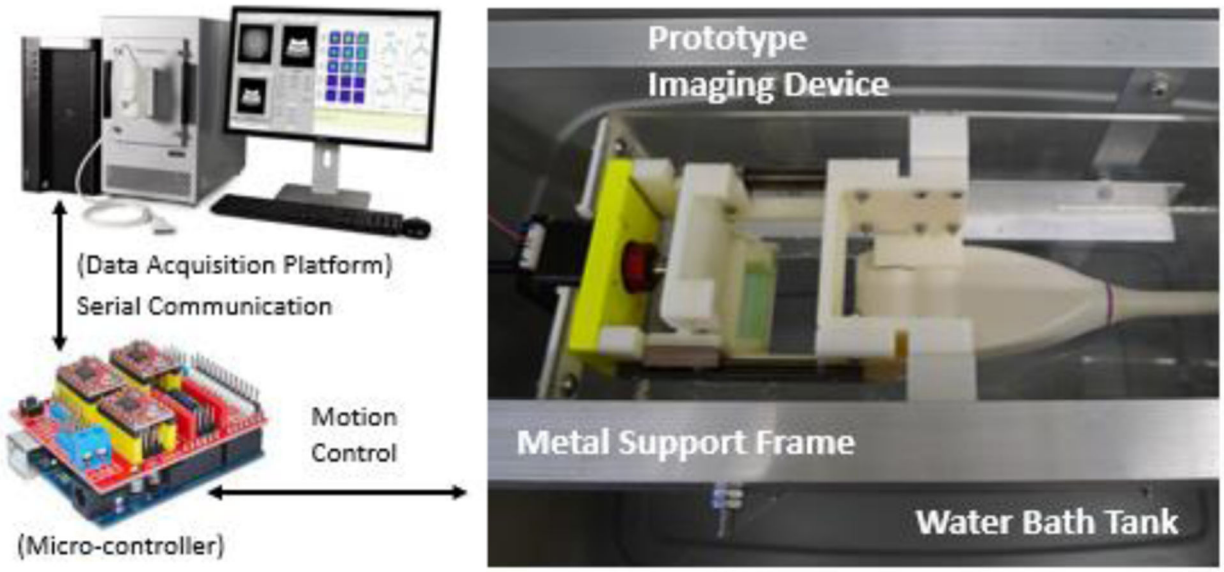

Fig. 5. Prototype 3D US imaging system.

Communication between data acquisition and motion control is implemented via serial portal. The imaging device is fixed using a metal frame and is partially submerged in a water bath.

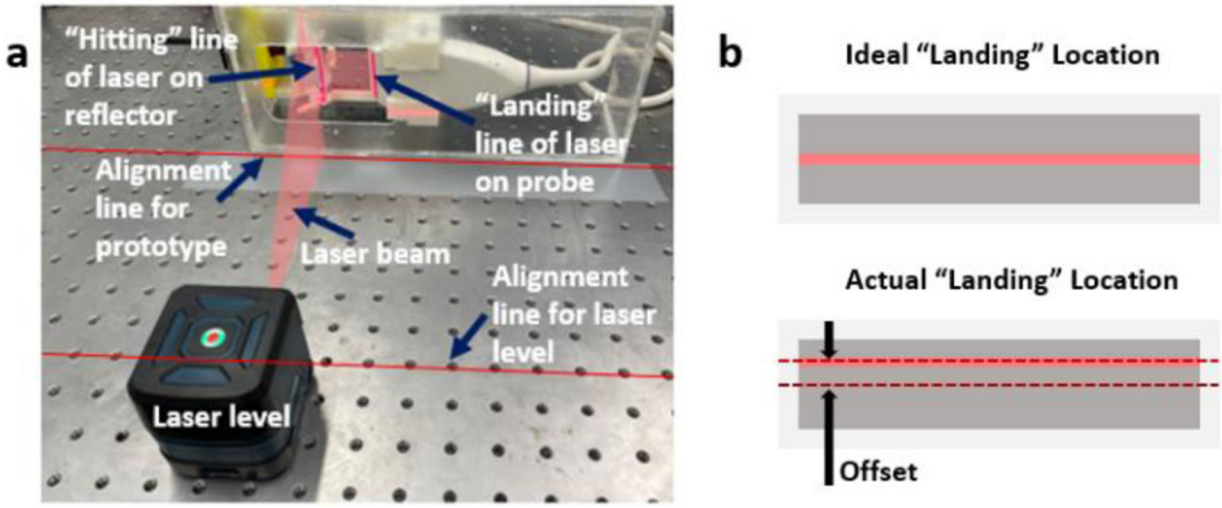

Fig. 6. Calibration of acoustic reflector angle.

(a) Reflector angle calibration setup with a laser level. (b) Ideal "landing" location of laser on the probe and existing offset.

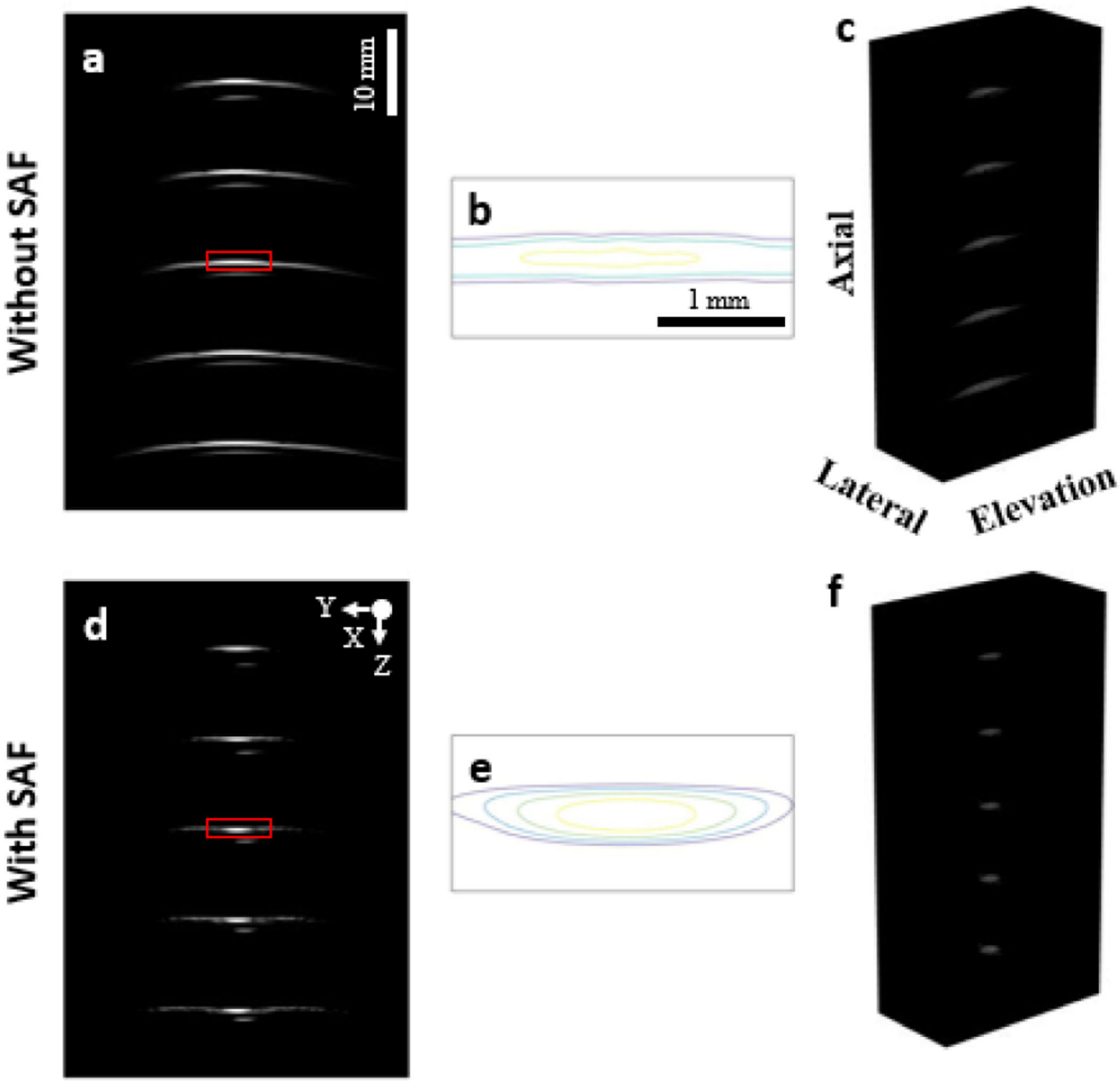

Fig. 7. Simulated PSF of point targets on elevation plane, dynamic range: 40 dB.

(a) Point targets without SAF on the central lateral position. (b) Contour plots of PSF without SAF at 27mm depth, the inner-most contour is at level of −3dB, and the interval between neighboring contours is 3dB. (c) 3D volume of PSF without SAF segmented at −20dB. (d) Point targets with SAF. (e) contour plots of PSF with SAF. (f) 3D volume of PSF with SAF.

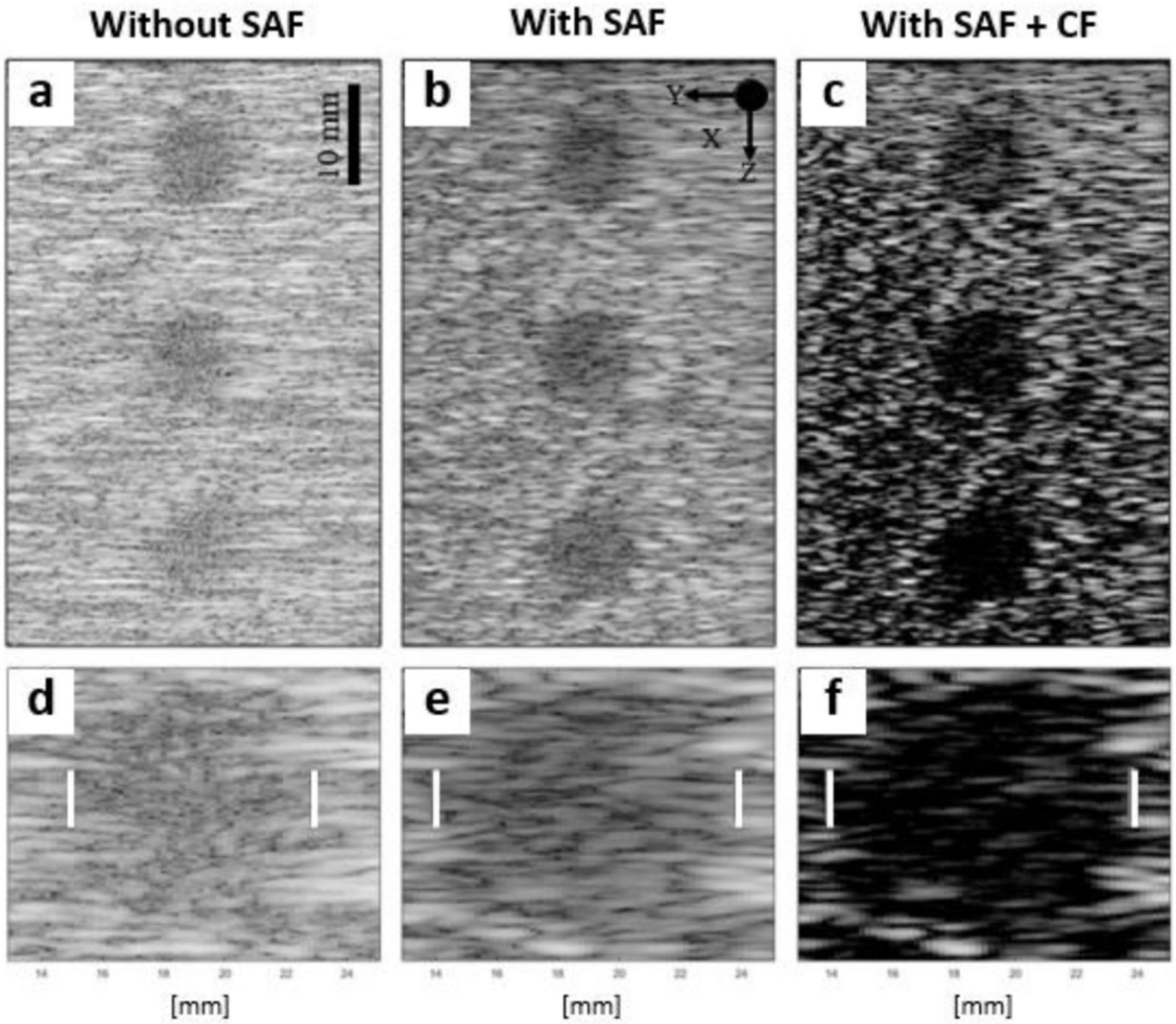

Fig. 8. Simulated cysts phantom on elevation plane, dynamic range: 60 dB.

(a) Cysts without SAF. (b) Cysts with SAF, delay-and-sum. (c) Cysts with SAF, with CF. (d)-(f) Enlarged cyst on the middle position in (a)-(c).

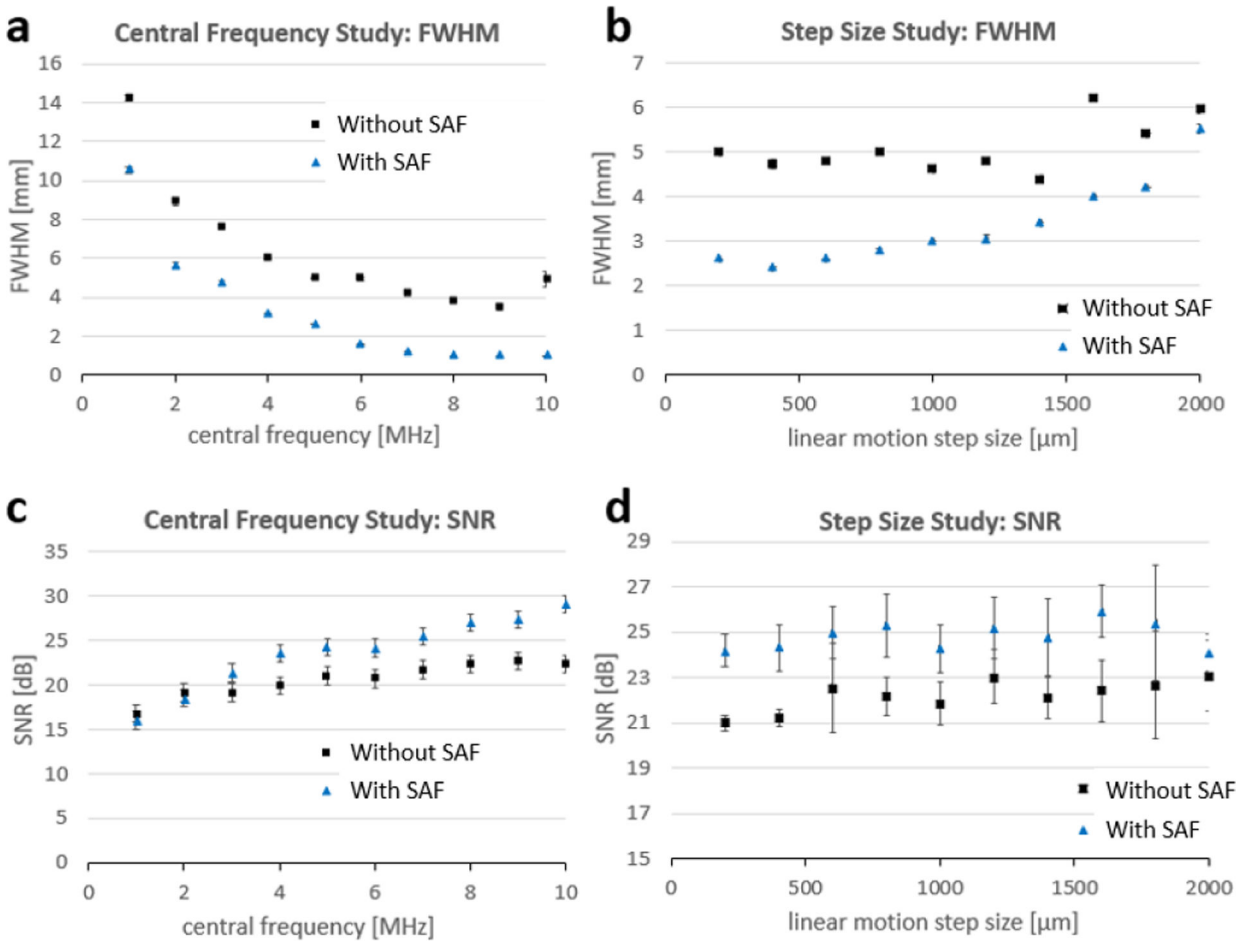

Fig. 9. Central frequency and motion step size optimization for SAF.

(a) FWHM of different central frequencies without and with SAF. (b) FWHM of different elevation step sizes. (c) SNR of different central frequencies. (d) SNR of different elevation step sizes.

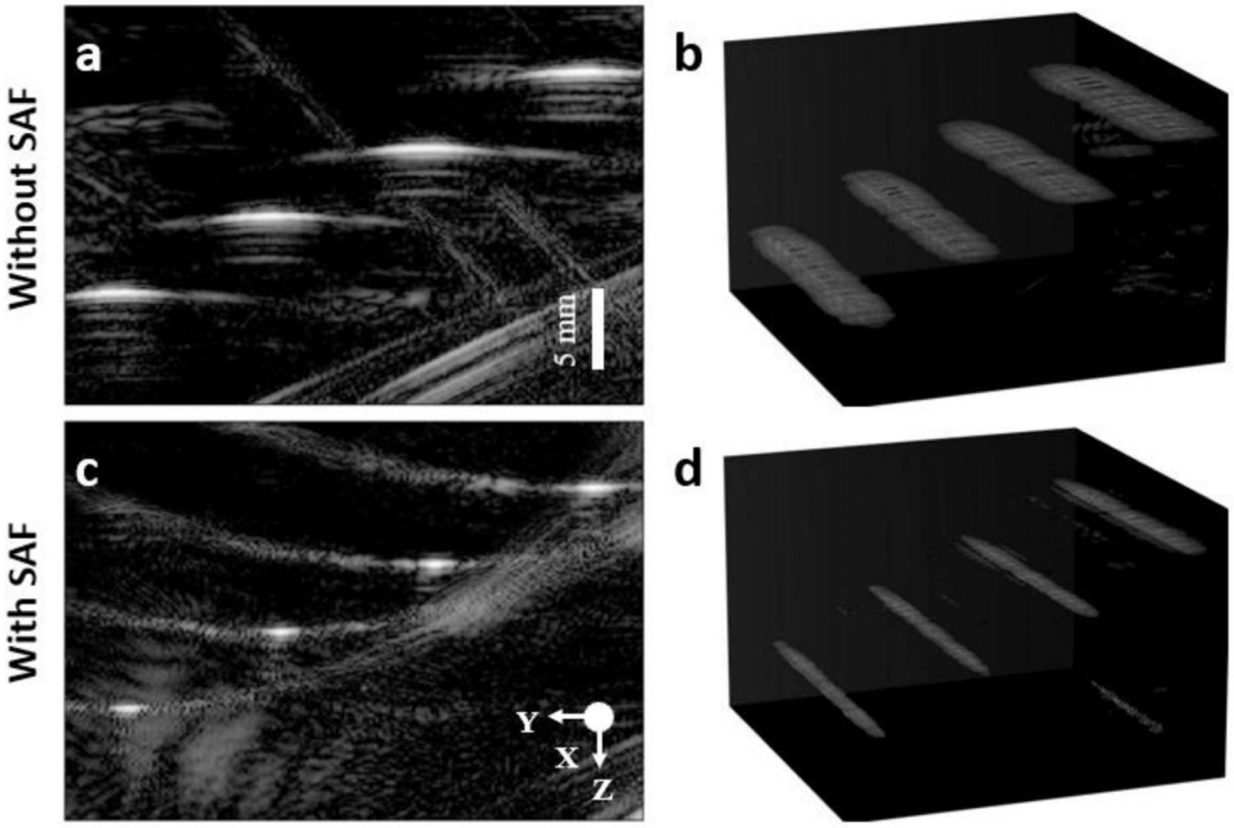

Fig. 10. Experimental data of wires phantom, dynamic range: 40 dB.

(a) Image of wires phantom on the elevation plane without applying SAF. (b) 3D visualization without SAF. (c) Image of wires phantom with SAF. (d) 3D visualization with SAF.

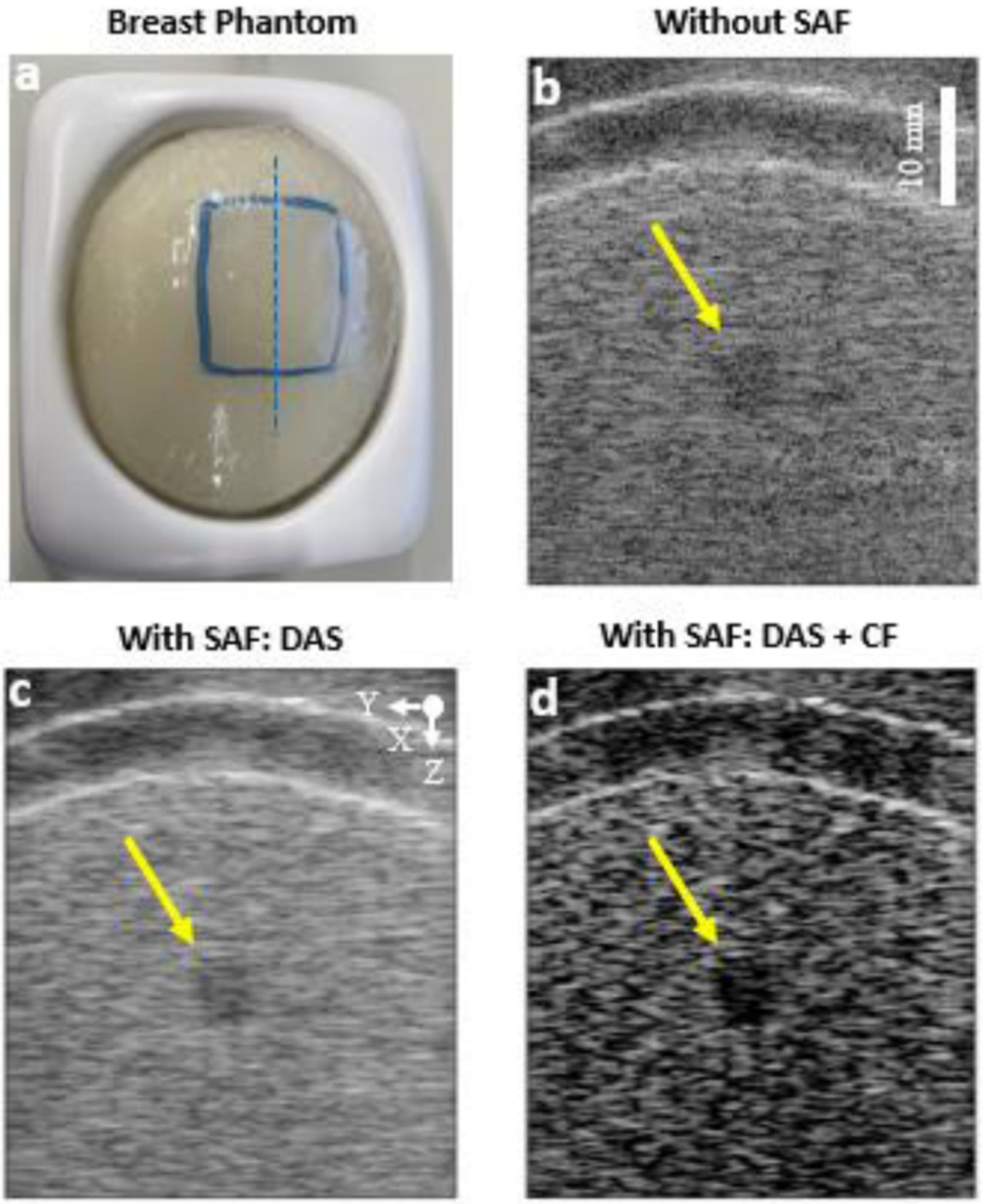

Fig. 11. Experimental data of breast phantom, dynamic range: 70 dB.

(a) Photo of the breast elastography phantom, with rectangle indicating scanned region and dashed line indicating the position of displayed 2D images. (b) Image of breast phantom without SAF. (c) Image of breast phantom with SAF, DAS. (d) Image of breast phantom with SAF, DAS with CF.

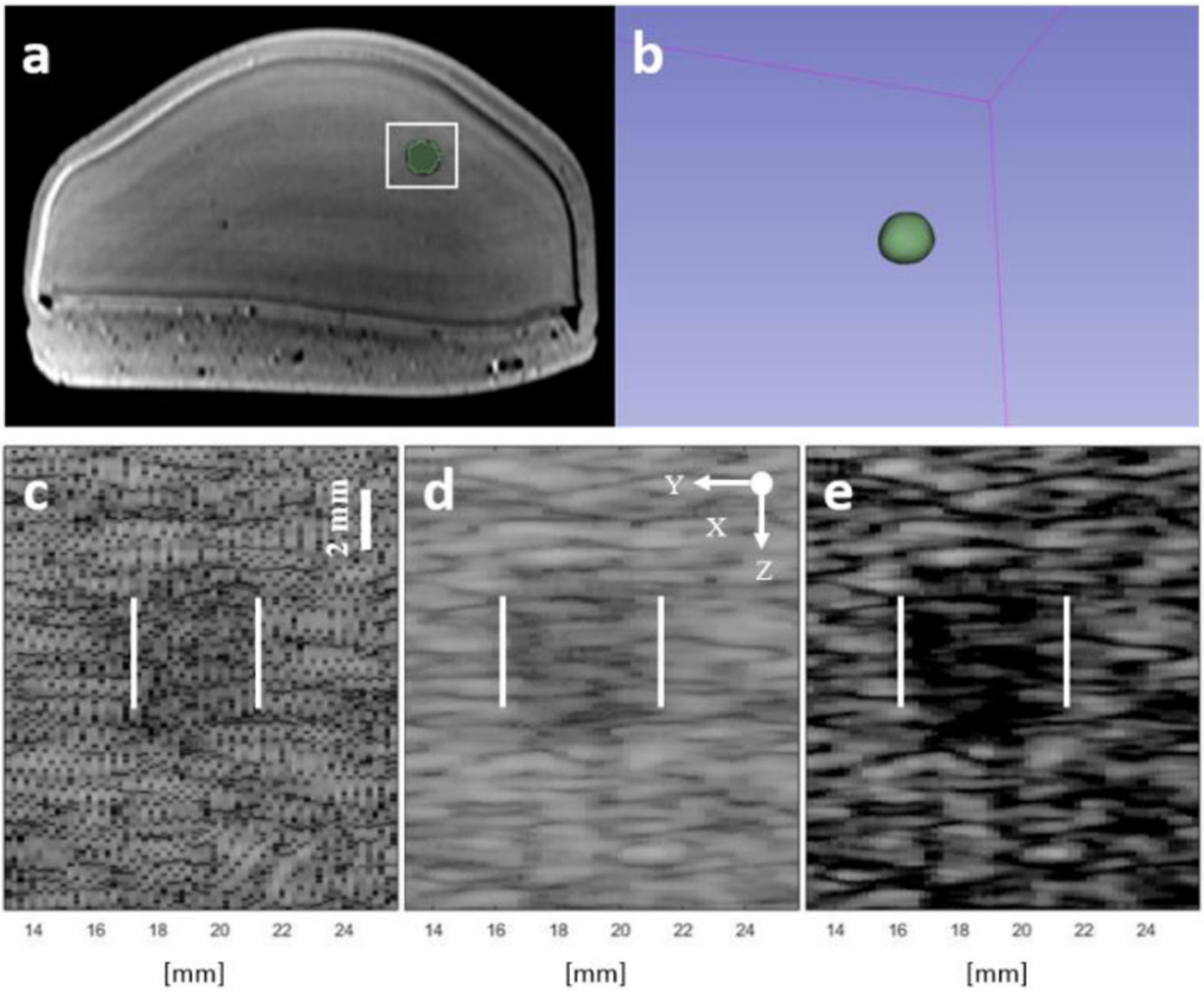

Fig. 12. Evaluation of breast phantom results.

(a) MRI image of the cyst region in interest. (b) Segmented cyst in 3D view. (c)-(e) Zoom-in cyst region in Figs. 11 (b)-(d).

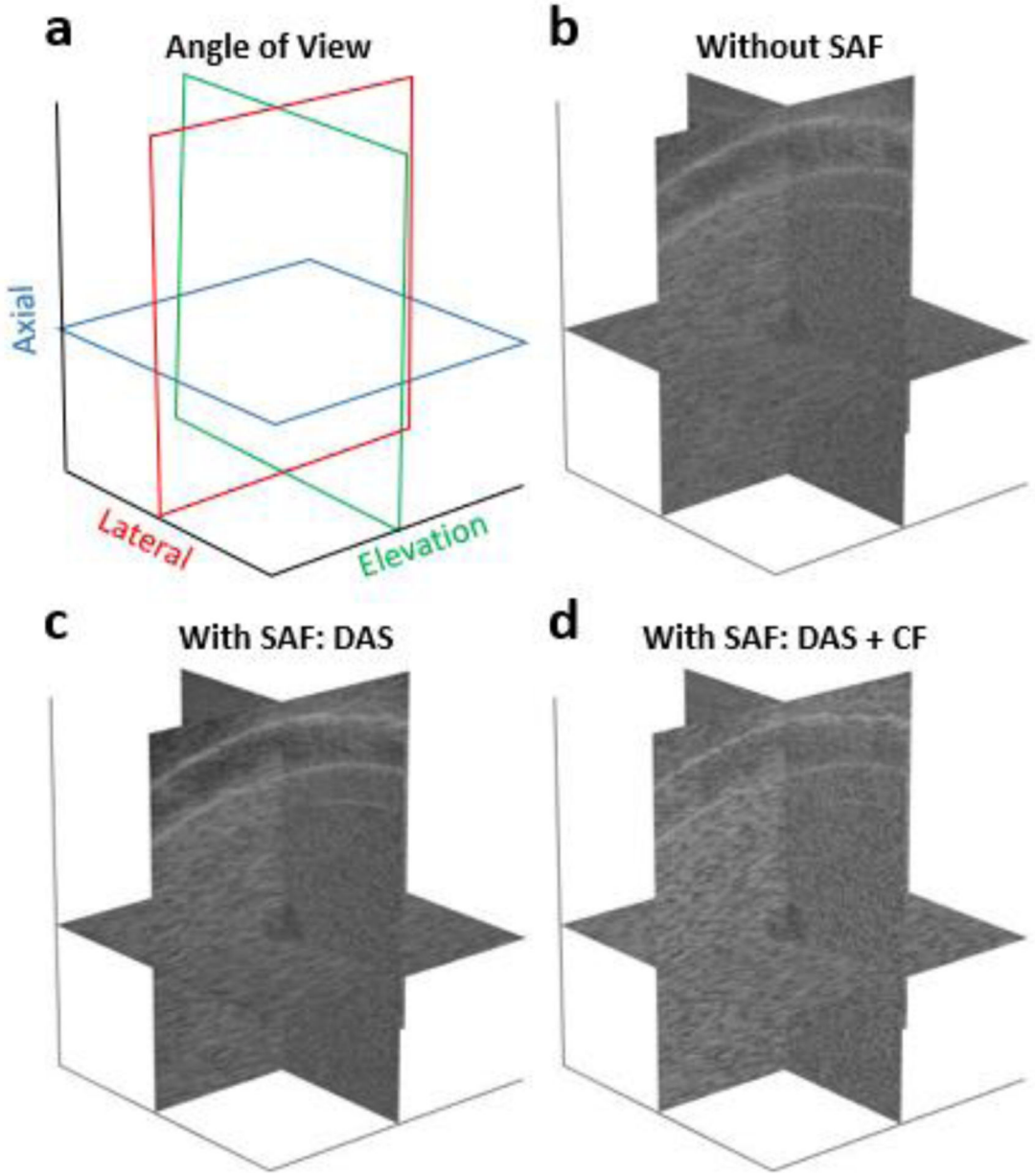

Fig. 13. 3D volume scanned from breast phantom, dynamic range 70 dB

(a) Angle of view of the 3D visualization. (b) 3D visualization of volume without SAF. (c) 3D visualization with SAF, DAS. (d) 3D visualization with SAF, DAS with CF.

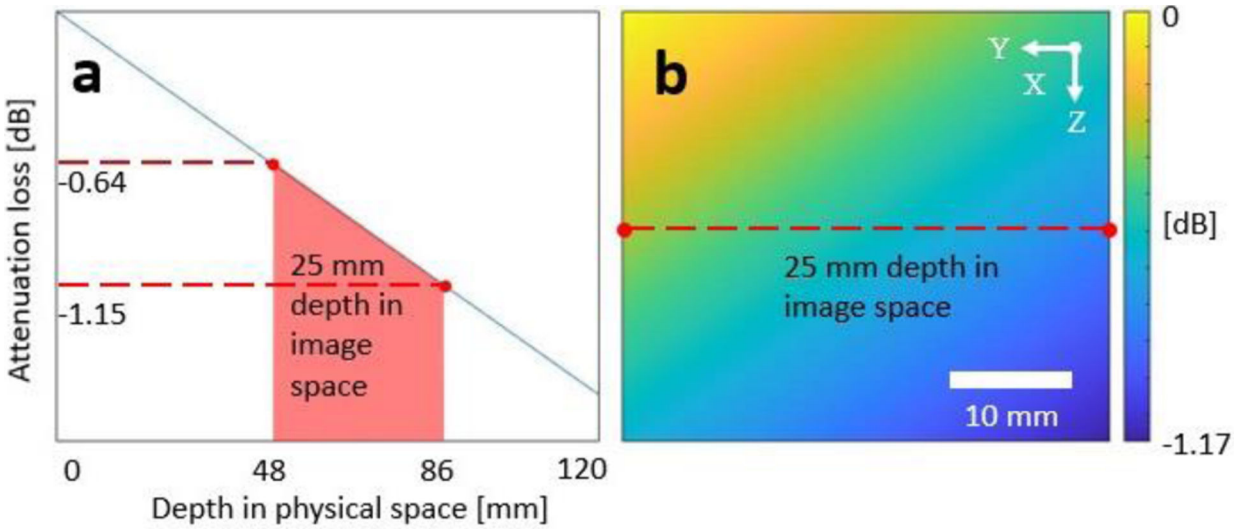

Fig. 14. Depth-dependent attenuation in the proposed imaging mechanism.

(a) Phenomenological model of amplitude attenuation as a function of depth (the red highlighted region corresponds to 25mm depth in image space). (b) Distribution of attenuation loss over the entire elevation FOV (the red light corresponds to 25mm in image space).

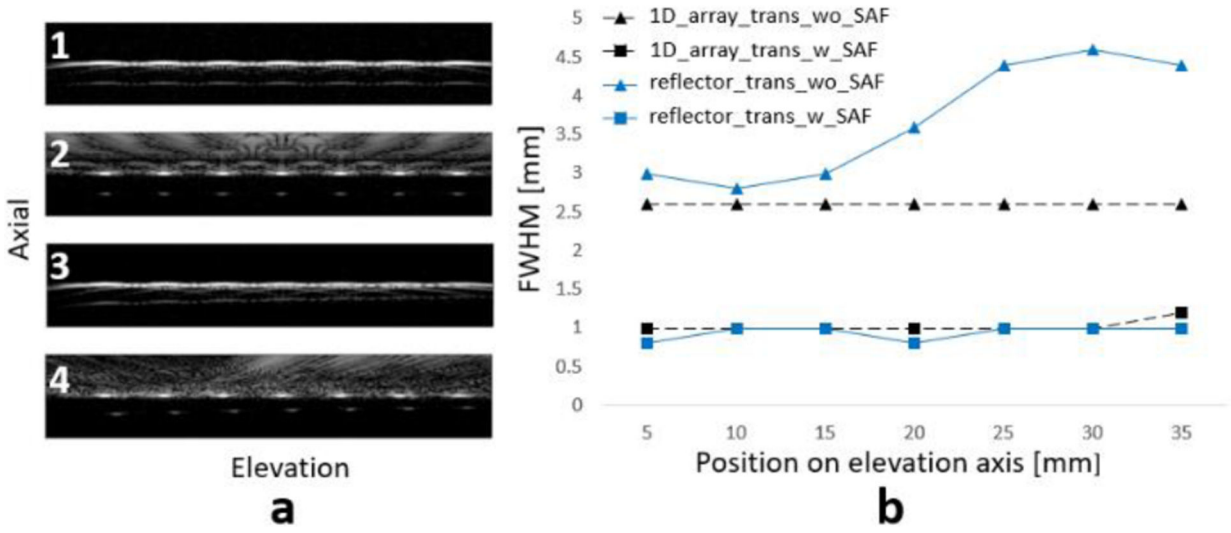

Fig. 15. Resolution deterioration in reflector-integrated elevation translation and compensation with SAF.

(a) 1. 1D array elevation translation, without SAF, 2. 1D array elevation translation, with SAF, 3. Reflector-integrated elevation translation, without SAF, 4. Reflector-integrated elevation translation, with SAF, dynamic range is 40 dB for all images. (b) FWHMs in four cases.

TABLE 1

Simulation Study Parameters

Parameters	Notation	Value	Unit
Speed of sound	C	1480	m/s
Central freq.	f_o	5	MHz
Sampling freq.	f_s	40	MHz
Num. elements	N_{xdc}	192	-
Element pitch	p	197.9	μm
Element kerf	$ker f$	25	μm
Element height	h	4.5	mm
Elevation focus	f	20	mm
Scan range	r	38	mm
Scan step	$\Delta\delta$	200	μm

TABLE 2

The quantified results of points and cysts simulations

FWHM and SNR of simulated PSF at 27 mm depth		
	Without SAF	**With SAF**
FWHM (mm)	4.98	2.60
SNR (dB)	42.00	48.38
CNR and measured diameter of simulated cyst at 30 mm depth		
CNR (*10^−2)	70.37	75.32
Diameter (mm)	8.00	10.00

TABLE 3

The quantified image quality of wires phantom

FWHM and SNR of four wires phantom on elevation plane		
Mean (Std.)	**Without SAF**	**With SAF, DAS**
FWHM (mm)	4.4 (0.35)	2.13 (0.61)
SNR (dB)	38.69 (4.01)	43.87 (3.70)

TABLE 4

The measured CNR and cyst diameter of the imaged breast phantom

Diameter of cyst on elevation plane, in the elevation direction		
	Without SAF	**With SAF, DAS**
CNR (* 10^−2)	1.06	1.75
Diameter (mm)	4.20	5.20
Percent error (%) (MRI ground truth: 7.14mm)	41.18	27.17